



# Measurement of the ratios of branching fractions $\mathcal{R}(D^*)$ and $\mathcal{R}(D^0)$

LHCb collaboration

## Abstract

The ratios of branching fractions  $\mathcal{R}(D^*) \equiv \mathcal{B}(\bar{B} \rightarrow D^* \tau^- \bar{\nu}_\tau) / \mathcal{B}(\bar{B} \rightarrow D^* \mu^- \bar{\nu}_\mu)$  and  $\mathcal{R}(D^0) \equiv \mathcal{B}(B^- \rightarrow D^0 \tau^- \bar{\nu}_\tau) / \mathcal{B}(B^- \rightarrow D^0 \mu^- \bar{\nu}_\mu)$  are measured, assuming isospin symmetry, using a sample of proton-proton collision data corresponding to  $3.0 \text{ fb}^{-1}$  of integrated luminosity recorded by the LHCb experiment during 2011 and 2012. The tau lepton is identified in the decay mode  $\tau^- \rightarrow \mu^- \nu_\tau \bar{\nu}_\mu$ . The measured values are  $\mathcal{R}(D^*) = 0.281 \pm 0.018 \pm 0.024$  and  $\mathcal{R}(D^0) = 0.441 \pm 0.060 \pm 0.066$ , where the first uncertainty is statistical and the second is systematic. The correlation between these measurements is  $\rho = -0.43$ . Results are consistent with the current average of these quantities and are at a combined 1.9 standard deviations from the predictions based on lepton flavor universality in the Standard Model.

Submitted to Phys. Rev. Lett.



Semileptonic  $b$ -hadron decays provide a powerful laboratory for testing the equality of the couplings of the three charged leptons to the gauge bosons, a fundamental characteristic of the Standard Model (SM), known as lepton flavor universality (LFU). Measurements of the LFU-sensitive ratios of branching fractions  $\mathcal{R}(D^*) \equiv \mathcal{B}(\bar{B} \rightarrow D^* \tau^- \bar{\nu}_\tau) / \mathcal{B}(\bar{B} \rightarrow D^* \ell^- \bar{\nu}_\ell)$ , where  $D^*$  indicates either  $D^{*+}$  or  $D^{*0}$  and  $\ell$  indicates a light lepton,<sup>1</sup>  $\mathcal{R}(D) \equiv \mathcal{B}(\bar{B} \rightarrow D \tau^- \bar{\nu}_\tau) / \mathcal{B}(\bar{B} \rightarrow D \ell^- \bar{\nu}_\ell)$  [1–7], where  $D$  indicates  $D^+$  or  $D^0$ , and  $\mathcal{R}(J/\psi) \equiv \mathcal{B}(B_c^- \rightarrow J/\psi \tau^- \bar{\nu}_\tau) / \mathcal{B}(B_c^- \rightarrow J/\psi \mu^- \bar{\nu}_\mu)$  [8] show an excess of semitauonic decays over the SM predictions, whereas a measurement of  $\mathcal{R}(A_c^+) \equiv \mathcal{B}(A_b^0 \rightarrow A_c^+ \tau^- \bar{\nu}_\tau) / \mathcal{B}(A_b^0 \rightarrow A_c^+ \mu^- \bar{\nu}_\mu)$  [9] is found to be consistent with the SM.

The LHCb collaboration has previously reported on LFU studies in the  $b \rightarrow c$  semileptonic decays using the data recorded during 2011–2012: two measurements of  $\mathcal{R}(D^{*+})$  using the purely leptonic tau decays  $\tau^- \rightarrow \mu^- \nu_\tau \bar{\nu}_\mu$  [2] and the hadronic decay channel  $\tau^- \rightarrow \pi^- \pi^+ \pi^- (\pi^0) \nu_\tau$  [5, 6], as well as measurements of the observables  $\mathcal{R}(J/\psi)$  in the leptonic channel [8] and  $\mathcal{R}(A_c^+)$  in the three-pion channel [9]. This Letter presents the first simultaneous measurement in hadron collisions of  $\mathcal{R}(D^*)$  and  $\mathcal{R}(D^0)$ , and supersedes the result of Ref. [2]. The data correspond to integrated luminosities of  $1.0 \text{ fb}^{-1}$  and  $2.0 \text{ fb}^{-1}$ , collected by the LHCb detector in proton-proton collisions with center-of-mass energies of 7 TeV and 8 TeV, respectively. Owing to the different spin structures of the  $\bar{B} \rightarrow D^* \ell^- \bar{\nu}_\ell$  and  $\bar{B} \rightarrow D \ell^- \bar{\nu}_\ell$  decays, the combined result provides significantly improved sensitivity to the structure of possible LFU-breaking processes originating from physics beyond the SM, including the effects of an extended Higgs mechanism or leptoquarks (see, *e.g.*, the recent review in Ref. [10]).

This study utilizes the purely leptonic tau decay  $\tau^- \rightarrow \mu^- \nu_\tau \bar{\nu}_\mu$  for the reconstruction of the semitauonic  $\bar{B} \rightarrow D^{(*)} \tau^- \bar{\nu}_\tau$  decays, where  $D^{(*)}$  stands for a  $D^0$ , a  $D^{*+}$  or a  $D^{*0}$  meson. These decays, hereafter denoted as the signal channels, as well as  $\bar{B} \rightarrow D^{(*)} \mu^- \bar{\nu}_\mu$  decays, which serve as the normalization for the determination of the  $\mathcal{R}(D^0)$  and  $\mathcal{R}(D^*)$  observables, are identified using the visible final states  $D^0 \mu^-$  and  $D^{*+} \mu^-$ . Both signal and normalization channels are selected by a common reconstruction procedure, which selects events containing a muon candidate and a  $D^0 \rightarrow K^- \pi^+$  candidate with the expected flavor correlation,  $D^0 \mu^-$ , from  $b \rightarrow c$  semileptonic decays. The sample is divided into  $D^0 \mu^-$  and  $D^{*+} \mu^-$  samples according to whether the combination of the  $D^0$  with any track in the event forms a  $D^{*+}$  candidate with a mass difference  $\Delta m < 160 \text{ MeV}/c^2$ , where  $\Delta m$  is the difference between the  $D^{*+}$  and  $D^0$  candidate masses.

The  $D^0 \mu^-$  sample contains contributions from  $B^- \rightarrow D^0 \tau^- \bar{\nu}_\tau$  and  $B^- \rightarrow D^0 \mu^- \bar{\nu}_\mu$  decays as well as contributions from partially reconstructed  $B^- \rightarrow D^{*0} \mu^- \bar{\nu}_\mu$ ,  $\bar{B}^0 \rightarrow D^{*+} \mu^- \bar{\nu}_\mu$ ,  $B^- \rightarrow D^{*0} \tau^- \bar{\nu}_\tau$ , and  $\bar{B}^0 \rightarrow D^{*+} \tau^- \bar{\nu}_\tau$  decays through the decay chains  $D^{*+} \rightarrow D^0 \pi^+$ ,  $D^{*0} \rightarrow D^0 \gamma$  and  $D^{*0} \rightarrow D^0 \pi^0$ , where the photon or pion is not reconstructed. The  $D^{*+} \mu^-$  candidate sample, which contains  $\bar{B}^0 \rightarrow D^{*+} \tau^- \bar{\nu}_\tau$  and  $\bar{B}^0 \rightarrow D^{*+} \mu^- \bar{\nu}_\mu$  and not the other signal or normalization decays, was the basis of the first measurement of  $\mathcal{R}(D^*)$  by the LHCb collaboration [2]. The simultaneous analysis of the two samples helps to constrain the common parameters of the fit models that are applied to the data, reducing the correlation between the measured values of  $\mathcal{R}(D^0)$  and  $\mathcal{R}(D^*)$ .

In addition to the signal and the normalization channels, the selected samples contain contributions from several background processes, which include: partially reconstructed  $B$  decays, such as semileptonic decays with an excited charmed meson and hadronic  $B$

---

<sup>1</sup>The inclusion of charge-conjugate processes is implied throughout this Letter.

decays into two charmed mesons, with one of them decaying (semi)leptonically; cases where the muon candidate originates from the misidentification of other charged particles; and combinations of unrelated particles from different decay chains. The kinematic and the topological properties of the various components are exploited to suppress background contributions. The relative contributions of the processes present in the data samples are determined by fitting to the data a model composed of multidimensional template distributions derived from control samples in data or from simulation validated against data.

The LHCb detector, described in detail in Refs. [11, 12], is a single-arm forward spectrometer covering the pseudorapidity range  $2 < \eta < 5$ , designed for the study of particles containing  $b$  or  $c$  quarks. The online event selection is performed by a trigger [13], which consists of a hardware stage, based on information from the calorimeter and muon systems, followed by a software stage, which applies a full event reconstruction. Simulation produced by software packages described in Refs. [14–19] is used to model the physics processes and the effects of both the detector acceptance and the selection criteria.

The events are required to pass the hardware trigger independently of the muon candidate, as the requirement in the hardware trigger on the component of the muon momentum transverse to the beam,  $p_T(\mu)$ , would significantly reduce the selection efficiency of the semitauonic decays. Therefore, the events must pass the hardware trigger either because the decay products of the  $D^0 \rightarrow K^-\pi^+$  candidate satisfy the hadron trigger requirements or because unrelated high- $p_T$  particles in the event satisfy any of the hardware trigger requirements. In the software trigger, the events are required to meet criteria designed to accept  $D^0 \rightarrow K^-\pi^+$  candidates with  $p_T > 2 \text{ GeV}/c$ . Quality requirements are applied to the tracks of the charged particles that originate from a candidate  $D^0$  decay: their momenta must exceed  $5 \text{ GeV}/c$  and at least one track must have  $p_T > 1.5 \text{ GeV}/c$ . The momentum vector of the  $D^0$  candidate must align approximately with the displacement from one of the primary vertices (PV) in the event and the reconstructed mass must be consistent with the known  $D^0$  mass [20].

In the offline reconstruction,  $K^-$  and  $\pi^+$  candidates from the  $D^0$  decay are required to satisfy loose particle identification requirements, and the decay vertex is required to be significantly separated from any PV. The invariant mass of the  $D^0$  candidate is required to be consistent with the  $D^0$  mass within three times the resolution, as determined by a fit to data. The muon candidate is required to be consistent with a muon signature in the detector, to have momentum  $3 < p < 100 \text{ GeV}/c$ , to be significantly separated from any PV, and to form a good vertex with the  $D^0$  candidate. To reduce further the background from hadrons misidentified as muons (“misID background”), muon likelihood-ratio identification criteria used previously [2] are supplemented with a dedicated multivariate selector, trained on information from multiple subdetectors, constrained to provide uniform efficiency in muon momentum and  $p_T$  using the uBoost method [21]. The  $D^0\mu^-$  combinations are required to have an invariant mass less than  $5280 \text{ MeV}/c^2$  and their momentum vector is required to align approximately with the displacement vector from the associated PV to the  $D^0\mu^-$  vertex, which removes random combinations while preserving a large fraction of semileptonic decays. In addition to the signal candidates, independent samples of “wrong sign” candidates,  $D^0\mu^+$ ,  $D^{*+}\mu^+$  and  $D^0\pi^-\mu^-$ , are selected for estimating the combinatorial background. The first two represent random combinations of  $D^{(*)}$  candidates with muons from unrelated decays, and the latter is used to model the contribution of misreconstructed  $D^{*+}$  decays. The

background from misreconstructed  $D^0 \rightarrow K^- \pi^+$  candidates is negligible. Mass regions  $5.28 < m(D^0 \mu^-) < 10 \text{ GeV}/c^2$  and  $\Delta m < 160 \text{ MeV}/c^2$  are included in all samples to study the combinatorial backgrounds.

To suppress the contributions from partially reconstructed  $B$  decays, the signal candidates are required to be isolated from additional tracks in the event. The isolation algorithm is described in Ref. [2]. Except for the muon identification procedure, the selection criteria for the  $D^{*+} \mu^-$  sample are unchanged from those used in Ref. [2].

Kinematic variables in the  $B$  candidate rest frame, approximated from the laboratory quantities by taking the  $B$  boost along the beam axis to be equal to that of the visible candidate [2], are used to characterize and discriminate between the various processes. These variables are: the muon energy in the  $B$  rest frame,  $E_\mu^*$ ; the missing mass squared, defined as  $m_{\text{miss}}^2 = (p_B - p_{D^{(*)}} - p_\mu)^2$ ; and the squared four-momentum transfer to the lepton system,  $q^2 = (p_B - p_{D^{(*)}})^2$ , where  $p_B$ ,  $p_{D^{(*)}}$  and  $p_\mu$  are the four-momenta of the  $B$  meson, the  $D^0$  (or  $D^{*+}$ ) meson and the muon.

Simulated events are used to derive the distributions of the  $B$  candidate rest-frame kinematic variables for the signal and the normalization channels as well as background from other partially reconstructed  $b$ -hadron decays. The sum of these multidimensional template distributions, which depends on shape parameters and the relative yields of the contributing processes, forms the fit model applied to the data. Two independent fit models and associated frameworks have been developed and applied to the data allowing for cross-checks on all aspects of the analysis.

The simulated samples of  $\bar{B} \rightarrow D^* \mu^- \bar{\nu}_\mu$  and  $\bar{B} \rightarrow D^* \tau^- \bar{\nu}_\tau$  decays are weighted to the BGL form-factor parameterization [22] using values presented in Refs. [23–25] as a starting point. For the decays  $B^- \rightarrow D^0 \mu^- \bar{\nu}_\mu$  and  $B^- \rightarrow D^0 \tau^- \bar{\nu}_\tau$ , form factors are described using the parameterization of Refs. [26, 27]. For the results presented here, the form factors are allowed to vary in the fit with only loose likelihood constraints for the parameters describing the helicity-suppressed form factors.

The backgrounds from semileptonic  $\bar{B}$  decays to the lowest-lying excited charm states  $D_1(2420)$ ,  $D_2^*(2460)$ ,  $D_1'(2430)$ , and  $D_0^*(2300)$  (collectively referred to as  $D^{**}$ ) are weighted to the form-factor parameterization presented in Ref. [28]. These form-factor parameters, which are allowed to vary without constraint in the fit, are constrained by control regions in the data, described below. Background from  $\bar{B}_s^0$  decays to the states  $D_{s1}(2536)^+$  and  $D_{s2}^*(2573)^+$ , (together denoted as  $D_s^{**}$ ) which subsequently decay as  $D_s^{**+} \rightarrow D^{*+} K^0$  or  $D_s^{**+} \rightarrow D^0 K^+$ , are modeled using the same form-factor parameterization, with values unconstrained and independent of those for the  $D^{**}$  states. Backgrounds from semileptonic  $B$  decays to heavier excited charm states  $D_{\text{heavy}}^{**}$  decaying as  $D_{\text{heavy}}^{**} \rightarrow D^{(*)} \pi \pi$  are modeled using simulated samples containing a mix of final states generated with the ISGW2 [29] form factors. As the composition and decay properties of this background are not well understood, an ad-hoc weight is applied as a linear function of the true  $q^2$  with independent slopes for decays to  $D^{*+}$ ,  $D^{*0}$ , and  $D^0$  which vary in the fit and are constrained by control regions in the data.

For the background from  $B$  decays into two charmed mesons, simulated samples of  $\bar{B}^0$  and  $B^-$  decays  $B \rightarrow D^{*+} H_c X$  and  $B \rightarrow D^0 H_c X$  with a mix of final states are used, where  $H_c$  is a charm meson that decays (semi)leptonically, yielding a correct-sign secondary muon to combine with the  $D^0$  or  $D^{*+}$ , and  $X$  is any combination of light hadrons (*e.g.*, a  $K$  or  $K^*$  meson). The multibody decays are simulated uniformly in phase space. Control samples (discussed below) are included to constrain corrections applied to the decay

distribution. The corrections involve weights given by linear and quadratic functions of the invariant mass of the two primary charm hadrons as well as variations of the size of the contribution of modes with  $m(X) > 680 \text{ MeV}/c^2$ , where the additional particles  $X$  are mostly  $K^*$  resonances. A separate sample is used to model the contribution from tertiary muons from  $H_c = D_s^{(*)-}$  with the leptonic decay  $D_s^- \rightarrow \tau^- \bar{\nu}_\tau$ .

To model the contribution of misID background, a control sample of  $D^0$  or  $D^{*+}$  candidates paired with a single track is used, where the combinations pass all the analysis selection criteria but the single track has no associated segment in the muon system. The two fit models employ two different techniques to produce a model of the misidentified backgrounds by weighting this control sample. Both techniques produce per-track weights using particle identification classification information on the extra track,  $\pi$ ,  $K$ ,  $p$ , or  $e$ , or unidentified, combined with particle identification efficiencies from large calibration samples. Details are given in the Supplemental Material [30]. Both techniques are independently validated by fitting data samples in which the muon candidate passes initial muon identification criteria, but fails to pass the custom multivariate muon identification developed for this analysis.

Combinatorial backgrounds are classified based on whether or not a genuine  $D^{*+} \rightarrow D^0 \pi^+$  decay is present. Wrong-sign  $D^0 \pi^- \mu^-$  combinations are used to determine the component with misreconstructed  $D^{*+}$  candidates. The size of this contribution is constrained by a fit to the  $\Delta m$  distribution of  $D^{*+} \mu^-$  candidates. The contribution from correctly reconstructed  $D^{*+}$  candidates combined with  $\mu^-$  from unrelated  $b$ -hadron decays is determined from wrong-sign  $D^{(*)} \mu^+$  combinations. In both cases, the contributions of misidentified muons are subtracted when generating the kinematic distributions for the fit. The mass region  $5.28 < m(D^{(*)} \mu^\mp) < 10 \text{ GeV}/c^2$  excludes genuine  $B$  decays, and is used to validate the agreement between the kinematic distributions for wrong-sign and correct-sign combinatorial background candidates.

Extensive studies are performed to account for differences between the data and the simulation. An initial set of corrections to the  $b$ -hadron production distributions is applied based on weights derived from the comparison of a sample of reconstructed  $B^+ \rightarrow J/\psi K^+$  decays in data and simulation. A sequence of additional corrections, as a function of kinematic and topological variables, is then applied to the simulation using a control sample of  $D^0 \mu^-$  candidates with  $m_{\text{miss}}^2 < 0.4 \text{ GeV}^2/c^4$ , which is dominated by the  $\bar{B} \rightarrow D^{(*)} \mu^- \bar{\nu}_\mu$  decay. Further corrections are applied using the corresponding region of the  $D^{*+} \mu^-$  sample to correct residual differences between data and simulation in the reconstruction of the low-momentum  $\pi^+$  in the  $D^{*+} \rightarrow D^0 \pi^+$  decay. This procedure is, in principle, iterative, but converges after a single round of corrections, and residual differences are covered in the systematic uncertainties discussed below.

In order to constrain the modeling of the various backgrounds presented above, several control regions enhanced in the background contributions are selected in both the  $D^0 \mu^-$  and  $D^{*+} \mu^-$  data based on the output of the isolation algorithm. Requiring the presence of a charged kaon candidate among the particles accompanying the  $D^{(0,*+)} \mu^-$  candidate results in a sample with an enhanced fraction of  $B$  decays into two charmed mesons. Samples enriched in semileptonic  $B$  decays to  $D^{**}$  are selected by requiring the presence of exactly one additional pion candidate in the vicinity of the  $D^{(0,*+)} \mu^+$  candidate with the correct relative charge for the  $D^{**} \rightarrow D^{(*)} \pi$  decay. Requiring exactly two accompanying pion candidates of opposite charge provides a sample with enhanced fraction of decays to  $D_{\text{heavy}}^{**}$  mesons. Including the isolated signal regions, eight regions are selected in total.

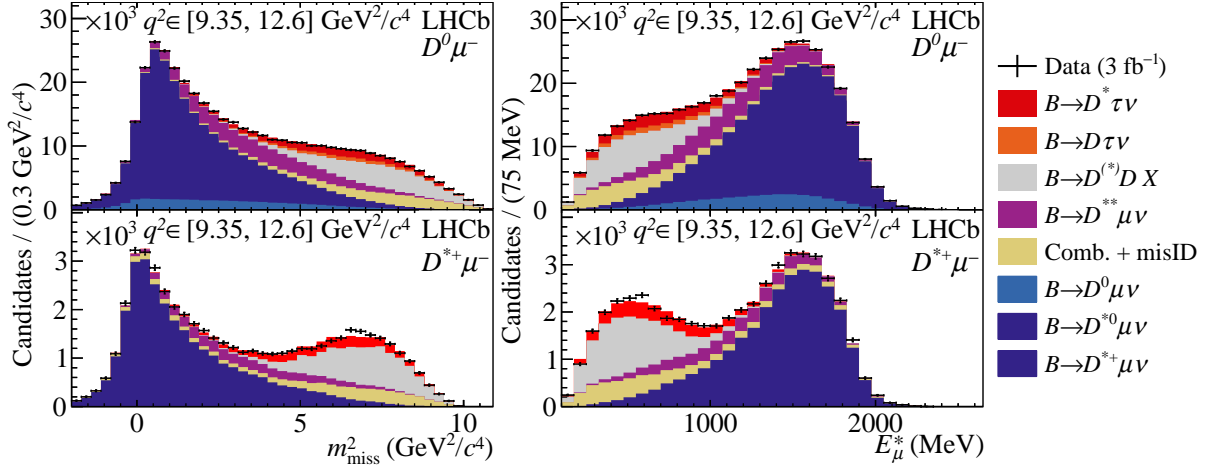


Figure 1: Distributions of (left)  $m_{\text{miss}}^2$  and (right)  $E_{\mu}^*$  in the highest  $q^2$  bin (above  $9.35 \text{ GeV}^2/c^4$ ) of the (top)  $D^0\mu^-$  and (bottom)  $D^{*+}\mu^-$  signal data, overlaid with projections of the fit model.

The binned distributions of  $m_{\text{miss}}^2$  ( $[-2, 10.6] \text{ GeV}^2/c^4$ , 43 bins),  $E_{\mu}^*$  ( $[100, 2650] \text{ MeV}$ , 34 bins), and  $q^2$  ( $[-0.4, 12.6] \text{ GeV}^2/c^4$ , 4 bins) for reconstructed  $D^0\mu^-$  and  $D^{*+}\mu^-$  candidates in data are fit using a binned extended maximum-likelihood method with three-dimensional templates representing the signal and normalization channels and the background sources. The model parameters extracted from the data include the yields of each contributing process: signals, normalizations,  $\bar{B} \rightarrow D^{**}\ell^- \bar{\nu}_{\ell}$  (with a Gaussian-constrained fraction of  $\bar{B} \rightarrow D^{**}\tau^- \bar{\nu}_{\tau}$ ),  $\bar{B} \rightarrow D_{\text{heavy}}^{**}\mu^- \bar{\nu}_{\mu}$ ,  $\bar{B}_s^0 \rightarrow D_s^{**}\mu^- \bar{\nu}_{\mu}$ ,  $\bar{B} \rightarrow D^{*+}H_c(\rightarrow \mu^- \bar{\nu}_{\mu} X')X$  (with a Gaussian-constrained fraction of  $\bar{B} \rightarrow D^{(*)}D_s^-(\rightarrow \tau^- \bar{\nu}_{\tau})X$ ), misID background, and combinatorial backgrounds. The form-factor parameters for signal, normalization, and  $D_{(s)}^{**}$  backgrounds are allowed to vary in the fit, as is the level of momentum smearing applied to the misID component to account for kaon or pion decays to muons. The same fit model is applied to all selected regions with appropriately selected templates, with form-factor parameters and shape correction parameters shared between regions, and yield parameters allowed to vary independently by region. Statistical uncertainties in the templates are folded into the likelihood via the Beeston-Barlow ‘lite’ prescription [31]. Projections of the fit in each control region are shown in the Supplemental Material [30].

Two approaches are used to incorporate the information from the control regions. For the result presented here, all eight regions are fit simultaneously using a custom likelihood implementation in the ROOT [32] software package to extract  $\mathcal{R}(D^0)$  and  $\mathcal{R}(D^*)$  including all correlations. In the alternative fit, built using the ROOFIT [33] and HISTFACTORY [34] frameworks, the six control regions are fit simultaneously first to obtain corrections to the most signal-like backgrounds in signal-depleted regions. The two signal samples are then fit with shapes fixed (or likelihood-constrained in the case of the  $\bar{B} \rightarrow D^{**}\mu^- \bar{\nu}_{\mu}$  and  $\bar{B}_s^0 \rightarrow D_s^{**}\mu^- \bar{\nu}_{\mu}$  form-factor parameters) according to the result of the control fit. The two fitters have been extensively cross-validated and give consistent results within an expected statistical spread determined using common pseudodatasets. As the two results are compatible, only the results of the former fit are presented in this Letter.

The results of the fit to the isolated (signal) samples are shown in Fig. 1. The complete set of projections for all  $q^2$  bins can be found in the Supplemental Material [30]. The ratios

Table 1: Absolute uncertainties in the extraction of  $\mathcal{R}(D^0)$  and  $\mathcal{R}(D^*)$ . The model uncertainties are divided into those included directly in the fit likelihood and those determined via supplemental studies.

<b>Internal fit uncertainties</b>	$\sigma_{\mathcal{R}(D^*)}(\times 10^{-2})$	$\sigma_{\mathcal{R}(D^0)}(\times 10^{-2})$	<b>Correlation</b>
Statistical uncertainty	1.8	6.0	-0.49
Simulated sample size	1.5	4.5	
$B \rightarrow D^{(*)}DX$ template shape	0.8	3.2	
$\bar{B} \rightarrow D^{(*)}\ell^{-}\bar{\nu}_\ell$ form-factors	0.7	2.1	
$\bar{B} \rightarrow D^{**}\mu^{-}\bar{\nu}_\mu$ form-factors	0.8	1.2	
$\mathcal{B}(\bar{B} \rightarrow D^*D_s^-(\rightarrow \tau^-\bar{\nu}_\tau)X)$	0.3	1.2	
MisID template	0.1	0.8	
$\mathcal{B}(\bar{B} \rightarrow D^{**}\tau^-\bar{\nu}_\tau)$	0.5	0.5	
Combinatorial	< 0.1	0.1	
Resolution	< 0.1	0.1	
<b>Additional model uncertainty</b>	$\sigma_{\mathcal{R}(D^*)}(\times 10^{-2})$	$\sigma_{\mathcal{R}(D^0)}(\times 10^{-2})$	
$B \rightarrow D^{(*)}DX$ model uncertainty	0.6	0.7	
$\bar{B}_s^0 \rightarrow D_s^{**}\mu^{-}\bar{\nu}_\mu$ model uncertainty	0.6	2.4	
Data/simulation corrections	0.4	0.8	
Coulomb correction to $\mathcal{R}(D^{*+})/\mathcal{R}(D^{*0})$	0.2	0.3	
MisID template unfolding	0.7	1.2	
Baryonic backgrounds	0.7	1.2	
<b>Normalization uncertainties</b>	$\sigma_{\mathcal{R}(D^*)}(\times 10^{-2})$	$\sigma_{\mathcal{R}(D^0)}(\times 10^{-2})$	
Data/simulation corrections	$0.4 \times \mathcal{R}(D^*)$	$0.6 \times \mathcal{R}(D^0)$	
$\tau^- \rightarrow \mu^- \nu \bar{\nu}$ branching fraction	$0.2 \times \mathcal{R}(D^*)$	$0.2 \times \mathcal{R}(D^0)$	
<b>Total systematic uncertainty</b>	2.4	6.6	-0.39
<b>Total uncertainty</b>	3.0	8.9	-0.43

of branching fractions are determined to be  $\mathcal{R}(D^0) = 0.441 \pm 0.060$ ,  $\mathcal{R}(D^*) = 0.281 \pm 0.018$ , with a correlation  $\rho = -0.49$ , where the statistical uncertainties are evaluated with all nuisance parameters related to template shape uncertainties fixed to their respective best-fit values. The normalization channel yields are 324 000  $\bar{B}^0 \rightarrow D^{*+}\mu^{-}\bar{\nu}_\mu$  decays in the  $D^{*+}\mu^{-}$  signal sample, and 354 000  $B^- \rightarrow D^0\mu^{-}\bar{\nu}_\mu$  decays, 958 000  $B^- \rightarrow D^{*0}\mu^{-}\bar{\nu}_\mu$  decays, and 44 000  $\bar{B}^0 \rightarrow D^{*+}\mu^{-}\bar{\nu}_\mu$  decays in the  $D^0\mu^{-}$  sample. The  $\bar{B}^0 \rightarrow D^{*+}\mu^{-}\bar{\nu}_\mu$  yield in the  $D^{*+}\mu^{-}$  sample is consistent with the previous measurement [2] after accounting for the efficiency of the stricter muon identification criteria used here.

Uncertainties in the measurements of  $\mathcal{R}(D^0)$  and  $\mathcal{R}(D^*)$  are summarized in Table 1. The uncertainty in extracting  $\mathcal{R}(D^{(*)})$  from the fit (model uncertainty) is dominated by the statistical uncertainty of the simulated samples; this contribution is estimated via the reduction in the fit uncertainty when the template statistical uncertainty is not considered in the likelihood. The systematic uncertainty from the kinematic shapes of the misID background is taken to be half the difference from using the two misID determination methods described above. Form-factor parameters are included in the likelihood as nuisance parameters, hence the associated systematic uncertainties are contained in the total uncertainties of  $\mathcal{R}(D^0)$  and  $\mathcal{R}(D^*)$  determined with all nuisance parameters allowed to vary. To determine the contribution of the form-factor uncertainty, the fit is repeated



with form-factor parameters fixed to their best-fit values, and the reduction in uncertainty compared with the configuration with varying nuisance parameters is used to determine the contribution from the form-factor uncertainties. The systematic uncertainty from empirical corrections to the kinematic distributions of  $\bar{B} \rightarrow D^{**}(\rightarrow D^{(*)}\pi\pi)\mu^-\bar{\nu}_\mu$  and  $\bar{B} \rightarrow D^{(*)}H_c(\rightarrow \mu\nu_\mu X')X$  backgrounds is computed in the same way.

The contribution of  $B \rightarrow D_{(s)}^{**}\tau^-\bar{\nu}_\tau$  decays relative to  $B \rightarrow D_{(s)}^{**}\mu^-\bar{\nu}_\mu$  is likelihood-constrained to an expectation of 8% taken from Ref. [28], with a relative uncertainty of 30% assigned to cover both the inclusion of different  $D_{(s)}^{**}\tau^-\bar{\nu}_\tau$  states, and the possibility of LFU violation in these decay modes. Similarly, the contribution of  $\bar{B} \rightarrow D^{(*)}D_s^-(\rightarrow \tau^-\bar{\nu}_\tau)X$  decays is likelihood-constrained using known branching fractions [20] with a 30% uncertainty. The systematic uncertainty is again given by the effect of allowing these to vary within the loose 30% constraint versus fixing them to best-fit.

The choice of corrections applied to simulated  $B \rightarrow D^{(*)}H_cX$  decays is not unique, and so the fit is repeated for an ensemble of possible alternative choices. The root mean square of this ensemble is taken as a systematic uncertainty.

A small discrepancy in the fit quality is observed in a region of the control samples dominated by cross-feed from  $\bar{B}_s^0 \rightarrow D_s^{**}\mu^-\bar{\nu}_\mu$  decays. To assess the maximum size of the effect from this mismodelling, a deformation which suppresses the low- $q^2$ , low- $E_\mu^*$  region of this template to better match the data is applied and the effect on the signal yield from this change is evaluated.

The default fit model does not include  $\Lambda_b^0 \rightarrow D^0 p\mu^-\bar{\nu}_\mu$  or  $\Lambda_b^0 \rightarrow D^{*+}n\mu^-\bar{\nu}_\mu$  decays. To assess the effect of their exclusion, a fit is performed to a control sample requiring a proton candidate among the particles accompanying the  $D^0\mu^-$  candidate. The existing  $\bar{B} \rightarrow D^{**}\mu^-\bar{\nu}_\mu$  simulated samples are reused with different parameter values as proxy for the  $\Lambda_b^0$  decays and are able to reproduce the kinematic distributions observed in the data. The fit for  $\mathcal{R}(D^{(*)})$  is repeated with these components included, and half the resulting shift is taken as a systematic uncertainty.

The expected yield of  $D^{(*)}\mu^-$  candidates compared to  $D^{(*)}\mu^+$  candidates (used to model the combinatorial background) varies as a function of  $m(D^{(*)}\mu^\mp)$ . The size of this effect is estimated in the  $5.28 < m(D^{(*)}\mu^\mp) < 10 \text{ GeV}/c^2$  region and the uncertainty is propagated as a systematic uncertainty in  $\mathcal{R}(D^{(*)})$ .

The systematic uncertainty due to the absence of the Coulomb interaction in the PHOTOS package [17] is evaluated by weighting the  $\bar{B}^0 \rightarrow D^{*+}\ell^-\bar{\nu}_\ell$  simulation by the Coulomb factor given in Ref. [35]. It is found that the only significant effect on these results is due to a 1% shift of the expected isospin relationship between  $\mathcal{R}(D^{*+})$  and  $\mathcal{R}(D^{*0})$ , which induces a small shift in  $\mathcal{R}(D^0)$  and  $\mathcal{R}(D^*)$ .

To assess the uncertainty from residual disagreements between data and simulation, a second iteration of the weighting procedure described above is performed using several possible variations of the scheme. Half the largest difference in  $\mathcal{R}(D^{(*)})$  is taken as a systematic uncertainty.

Uncertainties in converting the fitted ratio of signal and normalization yields into  $\mathcal{R}(D^{(*)})$  (normalization uncertainties) primarily come from the uncertainty in the effect of the corrections to simulation and are evaluated similarly. The uncertainty in the current world average value of  $\mathcal{B}(\tau^- \rightarrow \mu^-\bar{\nu}_\mu\nu_\tau)$  also contributes a small normalization uncertainty.

In conclusion, the branching fraction ratios  $\mathcal{B}(\bar{B} \rightarrow D^*\tau^-\bar{\nu}_\tau)/\mathcal{B}(\bar{B} \rightarrow D^*\mu^-\bar{\nu}_\mu)$  and

$\mathcal{B}(B^- \rightarrow D^0 \tau^- \bar{\nu}_\tau) / \mathcal{B}(B^- \rightarrow D^0 \mu^- \bar{\nu}_\mu)$  are measured to be  $0.281 \pm 0.018 \pm 0.024$  and  $0.441 \pm 0.060 \pm 0.066$ , respectively, with a correlation  $\rho = -0.43$ , where the first uncertainty is statistical and the second is systematic. This is the first measurement of the ratio  $\mathcal{R}(D^0)$  at a hadron collider. These results are consistent at less than one standard deviation with the current average of these quantities and stand at about two standard deviations from the predictions based on lepton flavor universality in the Standard Model.

## References

- [1] BaBar collaboration, J. P. Lees *et al.*, *Measurement of an excess of  $\bar{B} \rightarrow D^{(*)} \tau^- \bar{\nu}_\tau$  decays and implications for charged Higgs bosons*, Phys. Rev. **D88** (2013) 072012, [arXiv:1303.0571](#).
- [2] LHCb collaboration, R. Aaij *et al.*, *Measurement of the ratio of branching fractions  $\mathcal{B}(\bar{B}^0 \rightarrow D^{*+} \tau^- \bar{\nu}_\tau) / \mathcal{B}(\bar{B}^0 \rightarrow D^{*+} \mu^- \bar{\nu}_\mu)$* , Phys. Rev. Lett. **115** (2015) 111803, Publisher's Note *ibid.* **115** (2015) 159901, [arXiv:1506.08614](#).
- [3] Belle collaboration, M. Huschle *et al.*, *Measurement of the branching ratio of  $\bar{B} \rightarrow D^{(*)} \tau^- \bar{\nu}_\tau$  relative to  $\bar{B} \rightarrow D^{(*)} \ell^- \bar{\nu}_\ell$  decays with hadronic tagging at Belle*, Phys. Rev. **D92** (2015) 072014, [arXiv:1507.03233](#).
- [4] Belle collaboration, S. Hirose *et al.*, *Measurement of the  $\tau$  lepton polarization and  $R(D^*)$  in the decay  $\bar{B} \rightarrow D^* \tau^- \bar{\nu}_\tau$  with one-prong hadronic  $\tau$  decays at Belle*, Phys. Rev. **D97** (2018) 012004, [arXiv:1709.00129](#).
- [5] LHCb collaboration, R. Aaij *et al.*, *Measurement of the ratio of the  $\mathcal{B}(B^0 \rightarrow D^{*-} \tau^+ \nu_\tau)$  and  $\mathcal{B}(B^0 \rightarrow D^{*-} \mu^+ \nu_\mu)$  branching fractions using three-prong  $\tau$ -lepton decays*, Phys. Rev. Lett. **120** (2018) 171802, [arXiv:1708.08856](#).
- [6] LHCb collaboration, R. Aaij *et al.*, *Test of lepton flavor universality by the measurement of the  $B^0 \rightarrow D^{*-} \tau^+ \nu_\tau$  branching fraction using three-prong  $\tau$  decays*, Phys. Rev. **D97** (2018) 072013, [arXiv:1711.02505](#).
- [7] Belle collaboration, G. Caria *et al.*, *Measurement of  $\mathcal{R}(D)$  and  $\mathcal{R}(D^*)$  with a semileptonic tagging method*, Phys. Rev. Lett. **124** (2020) 161803, [arXiv:1910.05864](#).
- [8] LHCb collaboration, R. Aaij *et al.*, *Measurement of the ratio of branching fractions  $\mathcal{B}(B_c^+ \rightarrow J/\psi \tau^+ \nu_\tau) / \mathcal{B}(B_c^+ \rightarrow J/\psi \mu^+ \nu_\mu)$* , Phys. Rev. Lett. **120** (2018) 121801, [arXiv:1711.05623](#).
- [9] LHCb collaboration, R. Aaij *et al.*, *Observation of the decay  $\Lambda_b^0 \rightarrow \Lambda_c^+ \tau^- \bar{\nu}_\tau$* , Phys. Rev. Lett. **128** (2021) 191803, [arXiv:2201.03497](#).
- [10] F. U. Bernlochner, M. F. Sevilla, D. J. Robinson, and G. Wormser, *Semitauponic  $b$ -hadron decays: A lepton flavor universality laboratory*, Rev. Mod. Phys. **94** (2022) 015003, [arXiv:2101.08326](#).
- [11] LHCb collaboration, A. A. Alves Jr. *et al.*, *The LHCb detector at the LHC*, JINST **3** (2008) S08005.

- [12] LHCb collaboration, R. Aaij *et al.*, *LHCb detector performance*, Int. J. Mod. Phys. **A30** (2015) 1530022, arXiv:1412.6352.
- [13] R. Aaij *et al.*, *The LHCb trigger and its performance in 2011*, JINST **8** (2013) P04022, arXiv:1211.3055.
- [14] T. Sjöstrand, S. Mrenna, and P. Skands, *PYTHIA 6.4 physics and manual*, JHEP **05** (2006) 026, arXiv:hep-ph/0603175.
- [15] T. Sjöstrand, S. Mrenna, and P. Skands, *A brief introduction to PYTHIA 8.1*, Comput. Phys. Commun. **178** (2008) 852, arXiv:0710.3820.
- [16] D. J. Lange, *The EvtGen particle decay simulation package*, Nucl. Instrum. Meth. **A462** (2001) 152.
- [17] P. Golonka and Z. Was, *PHOTOS Monte Carlo: A precision tool for QED corrections in Z and W decays*, Eur. Phys. J. **C45** (2006) 97, arXiv:hep-ph/0506026.
- [18] Geant4 collaboration, J. Allison *et al.*, *Geant4 developments and applications*, IEEE Trans. Nucl. Sci. **53** (2006) 270.
- [19] Geant4 collaboration, S. Agostinelli *et al.*, *Geant4: A simulation toolkit*, Nucl. Instrum. Meth. **A506** (2003) 250.
- [20] Particle Data Group, R. L. Workman *et al.*, *Review of particle physics*, Prog. Theor. Exp. Phys. **2022** (2022) 083C01.
- [21] J. Stevens and M. Williams, *uBoost: A boosting method for producing uniform selection efficiencies from multivariate classifiers*, JINST **8** (2013) P12013, arXiv:1305.7248.
- [22] C. G. Boyd, B. Grinstein, and R. F. Lebed, *Precision corrections to dispersive bounds on form-factors*, Phys. Rev. **D56** (1997) 6895, arXiv:hep-ph/9705252.
- [23] D. Bigi and P. Gambino, *Revisiting  $B \rightarrow D\ell\nu$* , Phys. Rev. **D94** (2016) 094008, arXiv:1606.08030.
- [24] D. Bigi, P. Gambino, and S. Schacht,  *$R(D^*)$ ,  $|V_{cb}|$ , and the Heavy Quark Symmetry relations between form factors*, JHEP **11** (2017) 061, arXiv:1707.09509.
- [25] S. Jaiswal, S. Nandi, and S. K. Patra, *Extraction of  $|V_{cb}|$  from  $B \rightarrow D^{(*)}\ell\nu_\ell$  and the Standard Model predictions of  $R(D^{(*)})$* , JHEP **12** (2017) 060, arXiv:1707.09977.
- [26] HPQCD collaboration, H. Na *et al.*,  *$B \rightarrow D\ell\nu$  form factors at nonzero recoil and extraction of  $|V_{cb}|$* , Phys. Rev. **D92** (2015) 054510, arXiv:1505.03925.
- [27] C. Bourrely, I. Caprini, and L. Lellouch, *Model-independent description of  $B \rightarrow \pi\ell\nu$  decays and a determination of  $|V(ub)|$* , Phys. Rev. **D79** (2009) 013008, Erratum *ibid.* **D82** (2010) 099902, arXiv:0807.2722.
- [28] F. U. Bernlochner and Z. Ligeti, *Semileptonic  $B_{(s)}$  decays to excited charmed mesons with  $e, \mu, \tau$  and searching for new physics with  $R(D^{**})$* , Phys. Rev. **D95** (2017) 014022, arXiv:1606.09300.

- [29] D. Scora and N. Isgur, *Semileptonic meson decays in the quark model: An update*, Phys. Rev. **D52** (1995) 2783, [arXiv:hep-ph/9503486](#).
- [30] *See supplemental material at [link inserted by publisher] for further plots of signal and control regions, as well as a more detailed discussion of the modeling of non-muon background and a comparison to the previously published result., .*
- [31] R. J. Barlow and C. Beeston, *Fitting using finite Monte Carlo samples*, Comput. Phys. Commun. **77** (1993) 219.
- [32] R. Brun and F. Rademakers, *ROOT: An object oriented data analysis framework*, Nucl. Instrum. Meth. A **389** (1997) 81.
- [33] W. Verkerke and D. P. Kirkby, *The RooFit toolkit for data modeling*, eConf **C0303241** (2003) MOLT007, [arXiv:physics/0306116](#).
- [34] ROOT collaboration, K. Cranmer *et al.*, *HistFactory: A tool for creating statistical models for use with RooFit and RooStats* CERN-OPEN-2012-016, New York U., New York, 2012.
- [35] S. Calí, S. Klaver, M. Rotondo, and B. Sciascia, *Impacts of radiative corrections on measurements of lepton flavour universality in  $B \rightarrow Dlv_\ell$  decays*, Eur. Phys. J. **C79** (2019) 744, [arXiv:1905.02702](#).
- [36] M. Pivk and F. R. Le Diberder, *sPlot: A statistical tool to unfold data distributions*, Nucl. Instrum. Meth. **A555** (2005) 356, [arXiv:physics/0402083](#).
- [37] H. B. Prosper and L. Lyons, eds., *PHYSTAT 2011 Workshop on statistical issues related to discovery claims in search experiments and unfolding*, (Geneva), CERN, 2011. doi: 10.5170/CERN-2011-006.
- [38] F. Archilli *et al.*, *Performance of the muon identification at LHCb*, JINST **8** (2013) P10020, [arXiv:1306.0249](#).

# Supplemental Material

## A Detailed signal region fit projections

For compactness, Fig. 1 shows only the highest  $q^2$  region of the signal fit, where the signal purity is largest. The other  $q^2$  bins provide strong constraints on the non-signal contributions to the fit, as well as containing a substantial amount of signal themselves, albeit at a lower purity. Figures A.1 and A.2 show  $m_{\text{miss}}^2$  and  $E_\mu^*$  projections of the signal region of the fit for all  $q^2$  bins in order to provide a complete picture of the fit quality and completeness of the model.

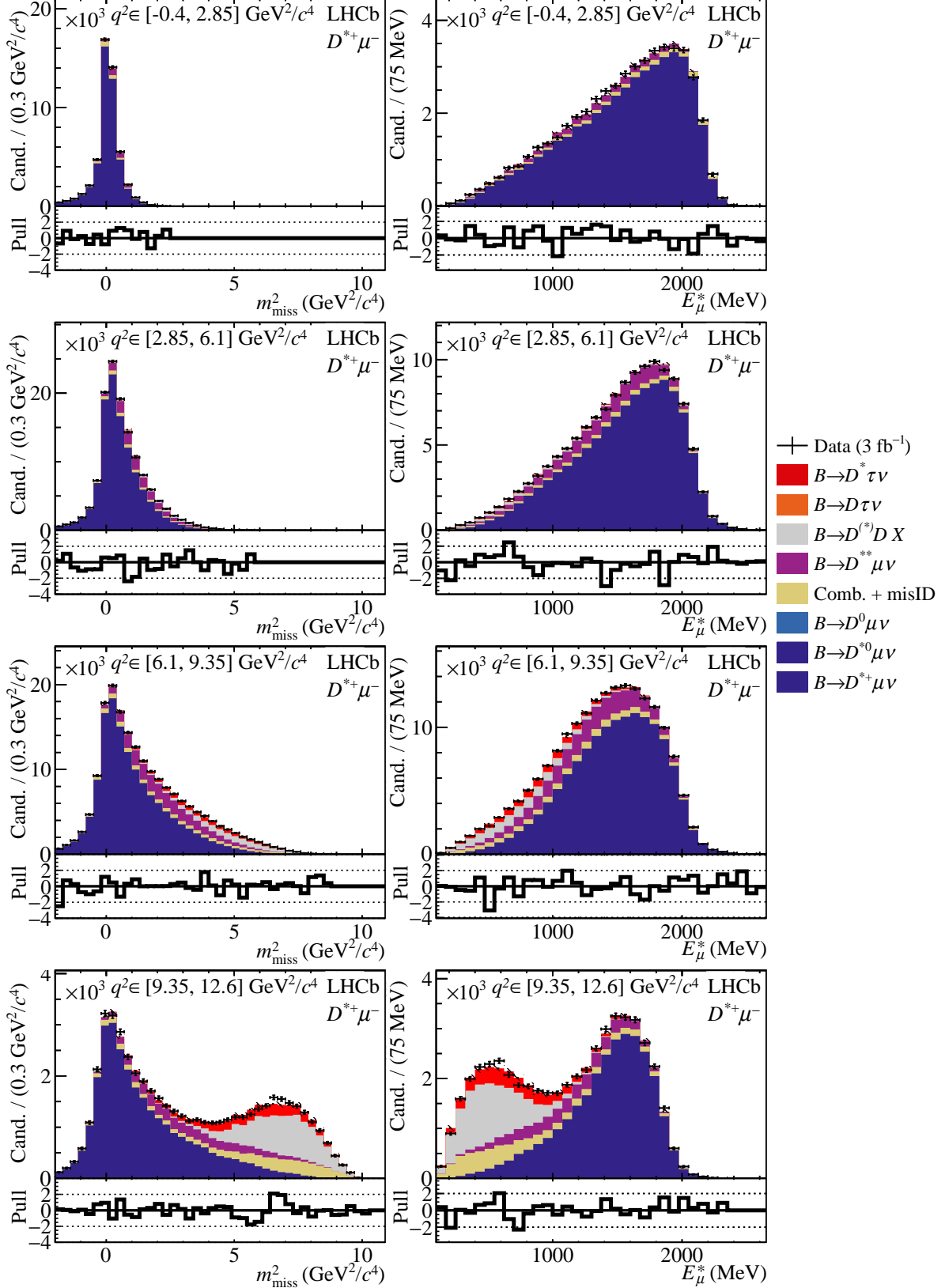


Figure A.1: Distributions of (left)  $m_{\text{miss}}^2$  and (right)  $E_{\mu}^*$  in each  $q^2$  bin of the  $D^{*+}\mu^-$  signal data, overlaid with projections of the fit model. Below each panel differences between the data and fit are shown, normalized by the summed statistical uncertainty of the data and simulation samples.

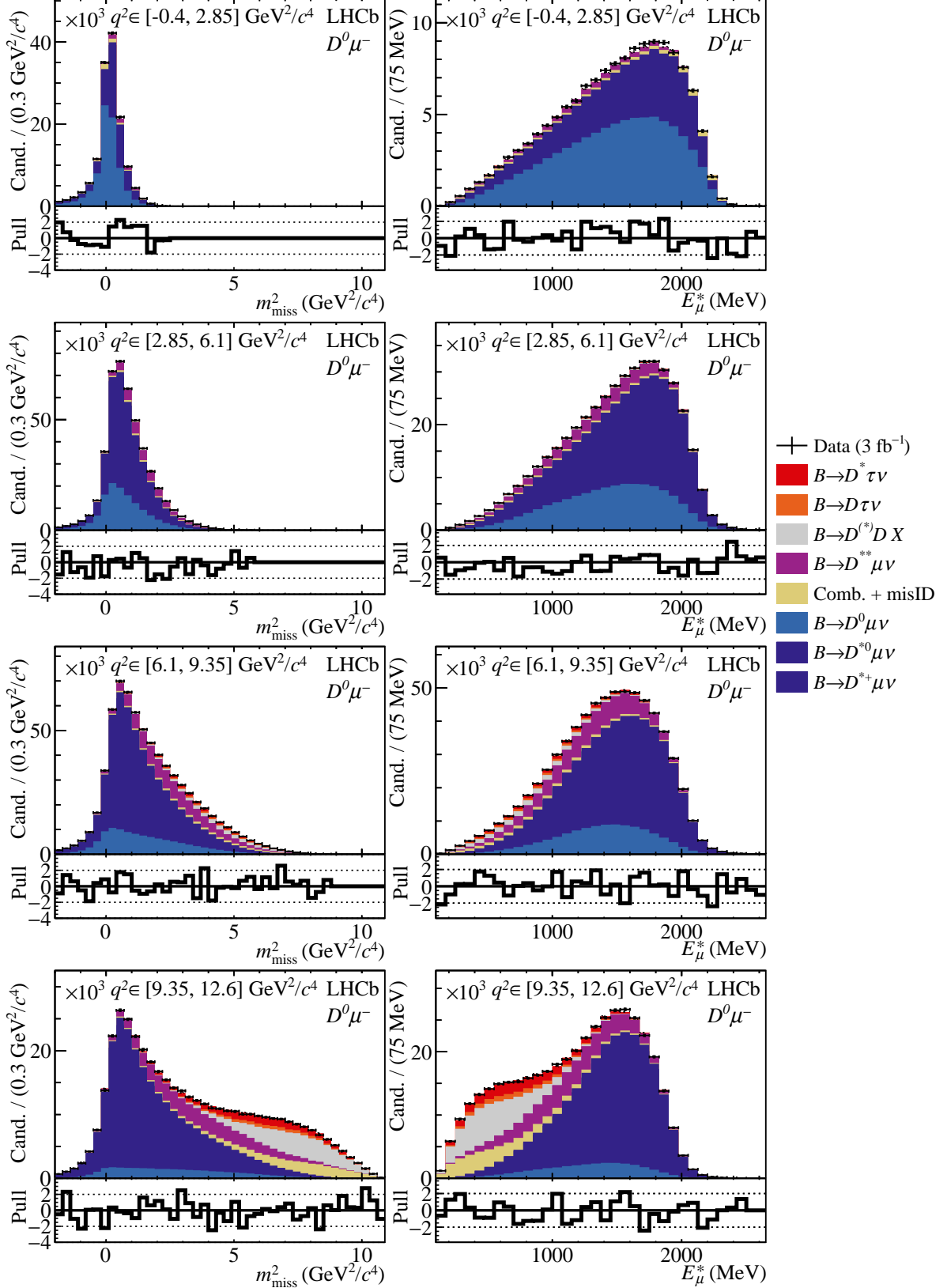


Figure A.2: Distributions of (left)  $m_{\text{miss}}^2$  and (right)  $E_{\mu}^*$  in each  $q^2$  bin of the  $D^0\mu^-$  signal data, overlaid with projections of the fit model. Below each panel differences between the data and fit are shown, normalized by the summed statistical uncertainty of the data and simulation samples.

## B Control region fit projections

As described in the text, the control regions selected to be fit simultaneously with the signal region are chosen to provide strong constraints on the modeling of the various parameters that determine the shapes of the backgrounds to the signal decays. These regions are fit using the same model as the signal region, but with templates derived from each of the respective selection regions. Figure B.3 shows the region with exactly one additional charge-correlated  $\pi$  candidate, Fig. B.4 shows the region with exactly two additional  $\pi$  candidates with opposite charge, and Fig. B.5 shows the region selected by the presence of a charged  $K$  candidate.

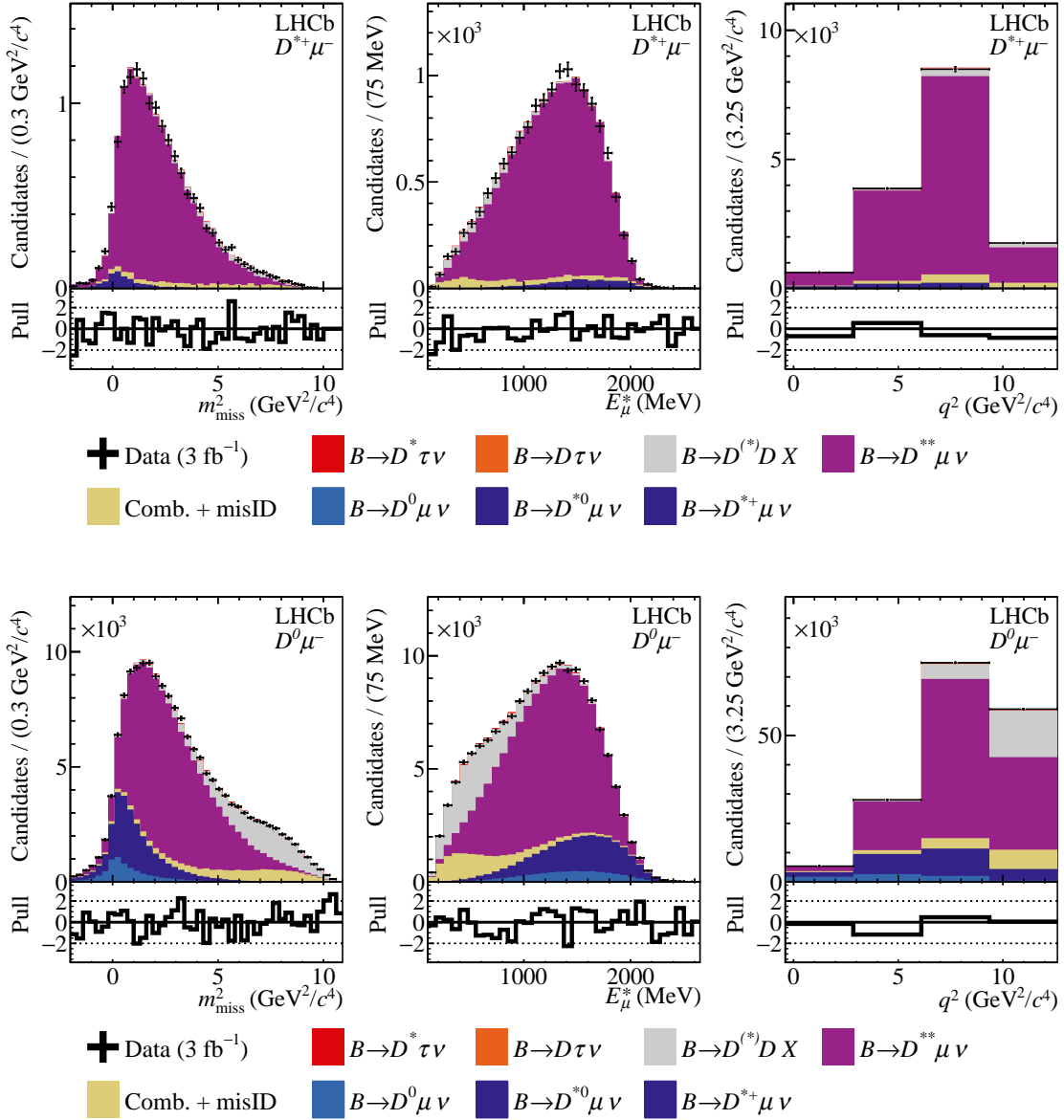


Figure B.3: Projections of the fit in (left) missing mass squared, (center) lepton energy, and (right)  $q^2$  in the (top)  $D^{*+}\mu^-$  and (bottom)  $D^0\mu^-$  region with exactly one extra pion consistent with the  $B$  vertex.



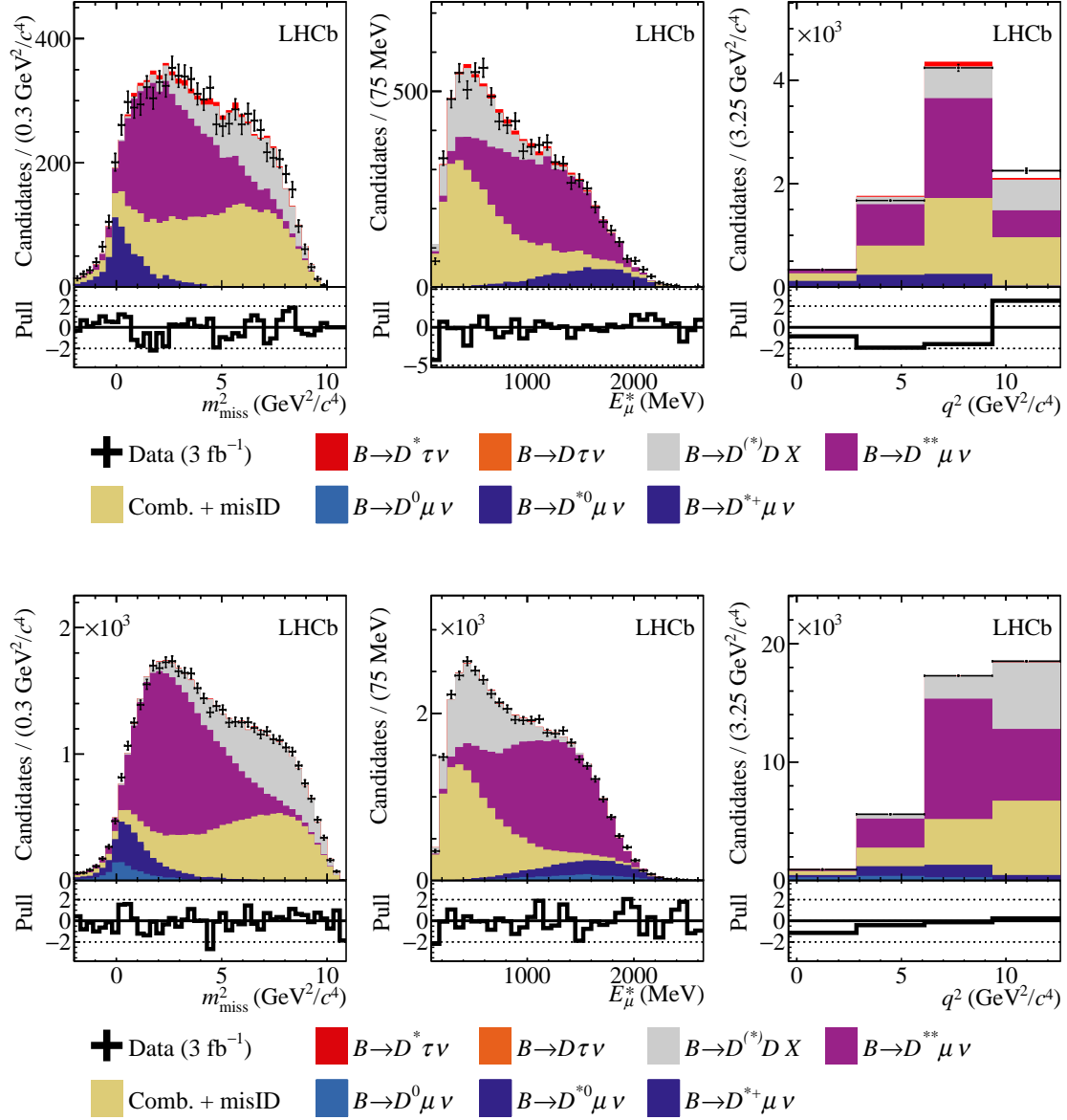


Figure B.4: Projections of the fit in (left) missing mass squared, (center) lepton energy, and (right)  $q^2$  in the (top)  $D^*\mu^-$  and (bottom)  $D^0\mu^-$  region with exactly two extra opposite-sign pions consistent with the  $B$  vertex.

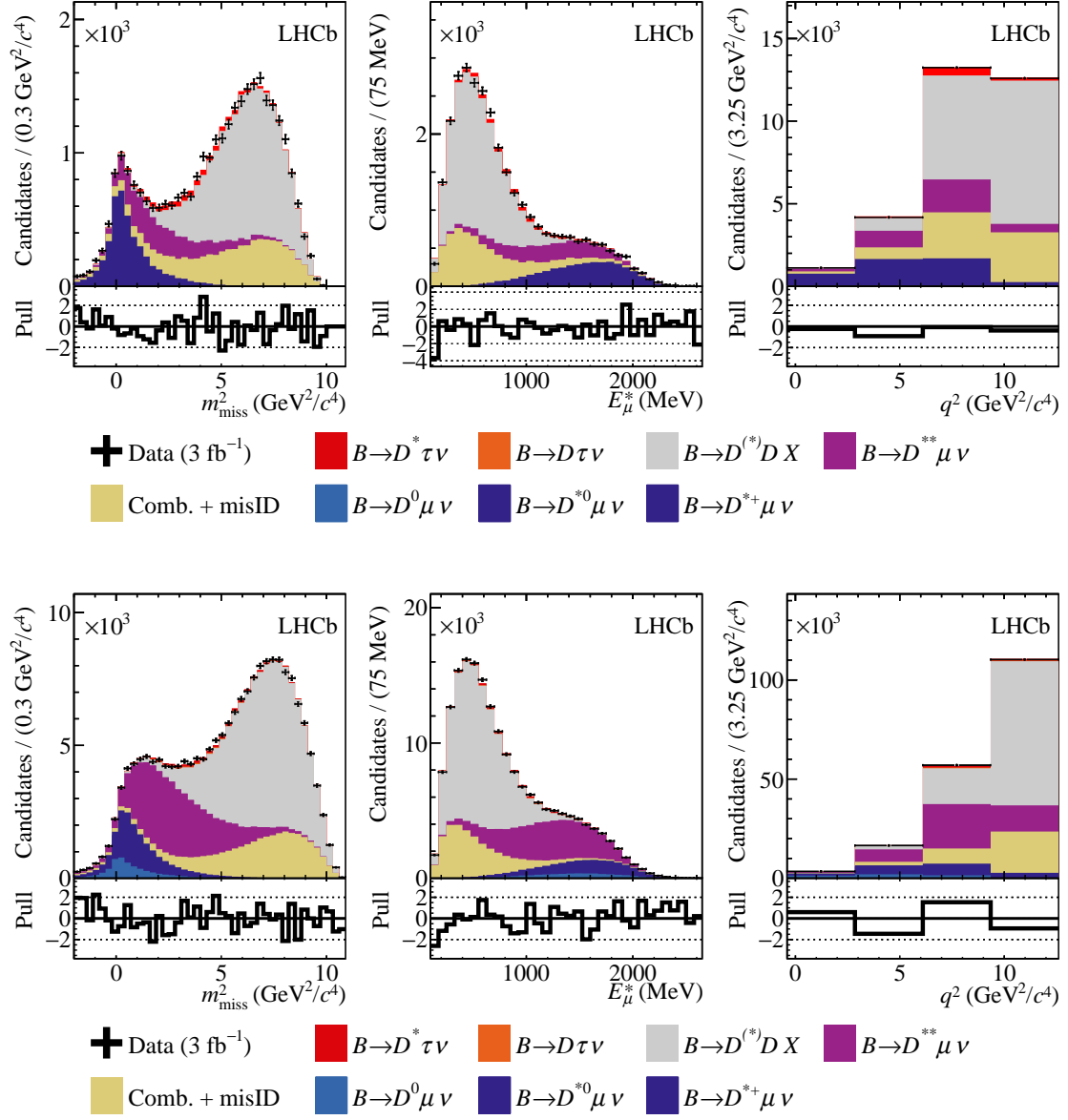


Figure B.5: Projections of the fit in (left) missing mass squared, (center) lepton energy, and (right)  $q^2$  in the (top)  $D^*\mu^-$  and (bottom)  $D^0\mu^-$  region with at least one kaon of either sign and no restrictions on the number of additional tracks consistent with the  $B$  vertex.

## C Determination of non-muon background using data

To model the contribution of misID background, a control sample of  $D^0$  or  $D^{*+}$  candidates paired with an extra track is used, where the combinations pass all the analysis selection criteria but the extra track taking the place of the muon has no associated segment in the muon system. Two techniques are used, corresponding with the two fitters developed for this analysis, with the goal of weighting this control sample to produce a model of the misidentified backgrounds.

In the first technique, used in the primary analysis reported here, the extra track in the  $D^*$ -track combination is categorized according to whether it passes particle identification (PID) criteria for  $\pi$ ,  $K$ ,  $p$ , or  $e$ , or whether it fails all four. The distribution of each identified particle species in a given kinematic bin may be fit using templates derived from large PID control samples. From these fits, *sWeights* [36] are produced to statistically separate the properties of the contribution from  $\pi$ ,  $K$ ,  $p$ ,  $e$  or misreconstructed tracks (“ghosts”). The *sWeights* are combined with muon misidentification rates measured in PID control samples to obtain per-track weights that, summed over all categories and all tracks, give a model of the misID background given the information in the  $D^*$ -track and PID control samples.

In the second technique, first employed in Ref. [8], the number of candidates passing each criteria as a function of track kinematics is used in conjunction with large PID calibration samples to unfold [37] the estimated true fraction of each species  $h$  ( $h = \pi, K, p, \text{ or } e$ , or misreconstructed “ghost” tracks) in a given kinematic bin. These unfolded numbers  $f_h$  are taken as prior probabilities that any given track’s true identity is one of the five species. The efficiencies for the category selections, measured in control data, are taken as conditional probabilities that a track of one true identity  $h$  is categorized as identity  $h'$ ,  $P(h'|h)$ . These two pieces of information may be combined using Bayes’s rule to obtain the probability  $P(h|h')$  that a track identified as  $h'$  has a given true identity  $h$ . These posterior probabilities are combined with muon misidentification rates from the PID calibration samples to produce a final weight for each track summed over the five hypotheses.

Due to the requirement that the tracks used in the misID modeling techniques fail muon identification criteria, there is no component of  $\pi$  or  $K$  decays in flight ( $\pi^+$  or  $K^+ \rightarrow \mu^+ \nu_\mu$ ) in the  $D^{(*)}$ -track sample used above. However, these are known to represent a significant contribution of the hadron to muon misidentification rate [38]. These decays in flight result in a mismeasurement of the “muon” momentum due to the deflection of the muon decay product with respect to the original  $\pi$  or  $K$  trajectory. This mismeasurement of the  $\pi$  or  $K$  momentum is included in the misID background model using a smearing derived from simulation. A simulated sample of  $D^0 \rightarrow K^- \pi^+$  is used, with muon identification criteria applied to either the kaon or the pion identical to the selection used in data. The mismeasurements of the track kinematics in this simulation sample are used to build an ensemble of possible momentum modifications, which are randomly sampled to build an ansatz for smearing the momenta of the  $D^{(*)}$ -track candidates. The exact amount of smearing is allowed to vary in the fit to the data to account for differences between this simulation and the misID background.

Both techniques for modeling the misID background are validated by fitting data

samples in which the muon candidate passes initial muon identification criteria, but fails to pass the custom multivariate muon identification developed for this analysis. This sample contains a higher number of misidentified muon candidates than are present in the signal samples, and tends to have a larger average momentum mismeasurement. The two techniques show excellent agreement with this sample once the smearing is applied.

## D Agreement with previous measurement

The  $D^{*+}\mu^{-}$  sample in this measurement overlaps completely with that previously analysed in Ref. [2]. To assess the level of agreement with the value of  $\mathcal{R}(D^*)$  in Ref. [2], a fit is performed to the  $D^{*+}\mu^{-}$  signal sample alone, with all shape parameters fixed to their best fit values from the default fit. The uncorrelated systematic uncertainty between the value of  $\mathcal{R}(D^*)$  from this fit and that in Ref. [2] is estimated from the quadratic difference in individual systematic uncertainties (excluding the misID unfolding, where 100% of the previous uncertainty is treated as uncorrelated, and the simulation statistical uncertainty where  $1/\sqrt{2}$  times the present uncertainty is assigned). The quadrature difference in statistical uncertainties is also included as the uncorrelated effect of the reduced statistical power of the data due to the more stringent muon identification requirements used here. This procedure gives an estimated uncorrelated uncertainty of 0.026 in  $\mathcal{R}(D^*)$ . The measured value of  $\mathcal{R}(D^*)$  in this fit is 0.293, in  $1.6\sigma$  agreement with Ref. [2].